Magnetic behavior of Ni nanoparticles and Ni2+ ions in weakly loaded zeolitic structures

Original
Magnetic behavior of Ni nanoparticles and Ni2+ ions in weakly loaded zeolitic structures / Barrera, G., Allia, P., Bonelli, B., Esposito, S., Freyria, F.S., Pansini, M., Marocco, A., Confalonieri, G., Arletti, R., Tiberto, P.. - In: JOURNAL OF ALLOYS AND COMPOUNDS. - ISSN 0925-8388. - 817:(2020), p. 152776. [10.1016/j.jallcom.2019.152776]

Publisher:
Elsevier Ltd

Published
DOI:10.1016/j.jallcom.2019.152776

Journal of Alloys and Compounds xxx (xxxx) 152776

Contents lists available at ScienceDirect

Journal of Alloys and Compounds

journal homepage: http://ees.elsevier.com

Magnetic behavior of Ni nanoparticles and Ni^{2+} ions in weakly loaded zeolitic structures

G. Barrera[a,*], P. Allia[a], B. Bonelli[b], S. Esposito[b], F.S. Freyria[b], M. Pansini[c], A. Marocco[c], G. Confalonieri[d], R. Arletti[e], P. Tiberto[a]

[a] INRIM, Advanced Materials Metrology and Life Sciences, Strada delle Cacce 91, I-10135, Torino, Italy
[b] DISAT, Politecnico di Torino and INSTM, Research Unit of Torino Politecnico, Corso Duca degli Abruzzi 24, I-10129, Torino, Italy
[c] Department of Civil and Mechanical Engineering and INSTM Research Unit, University of Cassino and Lazio Meridionale, via G. Di Biasio 43, 03043, Cassino, FR, Italy
[d] Department of Chemical and Geological Sciences, University of Modena and Reggio Emilia, Via Università 4, 41121, Modena, Italy
[e] Department of Earth Sciences, University of Torino, Via Valperga Caluso 35, I-10125, Torino, Italy

ARTICLE INFO

Article history:
Received 8 July 2019
Received in revised form 19 September 2019
Accepted 22 October 2019
Available online xxx

Keywords
Magnetic nanocomposites
Zeolites
Magnetic nanoparticles
Paramagnetic ions

ABSTRACT

Magnetic nanocomposites with low Ni content (nominal 1 wt%) were produced by a process involving thermal treatments of Ni-exchanged zeolite precursors of different type and investigated by XRPD, TEM and dc magnetic techniques. Ni-rich nanoparticles of size in the 10–80 nm range (depending on parent zeolite and thermal treatment) are observed at zeolite grain boundaries and/or surfaces, while a fraction f_0 of Ni^{2+} ions are present inside the grains. The blocking temperature of nanoparticles is above room temperature. At high temperatures ($75\,K \leq T \leq 300\,K$) the sample magnetization is dominated by nanoparticles; below, the paramagnetic signal of Ni^{2+} ions begins to be observed. A new procedure of magnetic data analysis is proposed and applied to find the residual ionic fraction f_0 in the two limit cases of full/no quenching of the orbital momentum on Ni^{2+} ions; f_0 turns out to be in the range 1.5–14.5%, depending on type of parent zeolite and thermal treatment. The temperature behavior of the high-field magnetization in the 2–300 K range and the variation of room-temperature magnetization are both explained taking into account the ionic and nanoparticle fractions estimated using the proposed method. Clustering of weakly interacting Ni^{2+} ions appears at low temperature in the sample with the highest ionic concentration.

1. Introduction

Magnetic nanocomposites obtained from zeolites of different type and consisting of a dispersion of transition metal (TM = Fe, Co, Ni) nanoparticles into an aluminosilicate matrix are the subject of active research in view of prospective, multifaceted applications including water remediation [1–3], treatment of pollutants [4–8] catalysis [9–12] and biomedicine [13,14].

These nanomaterials can be prepared through various different methods [15]. A technique recently proposed by some of us [16–19] is based on a smart, scalable process encompassing two simple operations: Fe^{2+}, Co^{2+}, or Ni^{2+} exchange of commercial zeolites followed by thermal treatment under a reducing atmosphere at relatively moderate temperatures (500–850 °C). This simple and rather inexpensive process typically results in a dispersion of magnetic nanoparticles into a prevailingly amorphous silica and alumina ceramic matrix deriving from the collapse of TM-exchanged zeolites by effect of furnace treatments. Magnetic metal-ceramic nanocomposites obtained in this way were already successfully used in the *Escherichia Coli* DNA separation [20], in pesticides removal from water by adsorption [21] and in the production of simulated moon agglutinates [22], obtaining encouraging results.

Explaining the magnetic properties of these nanocomposites is often a challenge because of their complex structure and morphology [23,24]. Recently, a detailed picture of magnetism in some metal-ceramic materials has been achieved by combining the results of magnetic measurements with the information about structure, composition and morphology [23].

Nanocomposites containing low (1–5%) fractions of magnetic metals are interesting for two orders of reasons: from the fundamentalist's viewpoint, a limited amount of exchanged magnetic ions may result in different end products and/or magnetic properties with respect to more intensively exchanged zeolites; furthermore, low TM contents can be functional in some applications such as DNA separation and water remediation [20,21].

This paper is devoted to study the magnetic properties of zeolitic materials obtained starting from A/X zeolites and containing a low nominal fraction of exchanged Ni ions (≅ 1 wt%). The magnetic behavior of the samples is interpreted by exploiting the information

---

* Corresponding author. INRIM, Strada delle Cacce 91, 10135, Torino, Italy
E-mail address: g.barrera@inrim.it (G. Barrera)

https://doi.org/10.1016/j.jallcom.2019.152776
0925-8388/© 2019.

about their structure and morphology. The magnetization is viewed as the sum of two concurrent magnetic contributions, from Ni-rich nanoparticles and from Ni^{2+} ions dispersed in the zeolite matrix, giving rise to a ferromagnetic and a paramagnetic signal, respectively. Field Cooled and Zero Field Cooled (FC/ZFC) low-field magnetization curves are dominated by the magnetic response of interacting nanoparticles. An *ad-hoc* technique of magnetic data analysis is introduced and applied in order to accurately estimate the amount of exchanged Ni belonging in each magnetic phase.

The present study shows that a careful analysis of magnetic measurements supported by the knowledge of chemical composition, structure and morphology can be particularly effective to get insight into fine chemical/compositional details of magnetic nanocomposites containing low amounts of magnetic species, which are typically beyond the sensitivity limits of standard characterization techniques such as X-ray diffraction and TEM image analysis.

2. Materials preparation

The studied magnetic metal-ceramic nanocomposites were prepared as follows: the parent A (Sigma Aldrich) and X (Carlo Erba) zeolites were contacted with a 0.00170 and 0.00143 M [Ni^{2+}] solution, respectively, at a wt. solid/liquid ratio of (S/L) = 1/100, at room temperature and contact time (t) = 2 h. The solid was separated from the liquid by filtration, and was subsequently washed in distilled water, dried for about one day at 80 °C, and stored for at least 3 days in an environment with about 50% relative humidity to allow water saturation of the zeolites. Cation-exchange operations have been described in Refs. [25–27]. In this case, a single exchange with the [Ni^{2+}] solution was done for both parent zeolites.

The Ni^{2+} exchanged A and X zeolites were submitted to thermal treatment in a reducing atmosphere (obtained by a flow of a 2% vol. H_2–Ar mixture) under the following conditions:

1) Heating from room temperature up to 735 °C (15 °C/min heating rate) and subsequent isothermal treatment for 12 min. After switching the heating system of the furnace off, the sample was cooled down to room temperature within the furnace (samples referred to as NiA735C-12min and NiX735C-12min).
2) Heating from room temperature up to 750 °C (15 °C/min heating rate). As soon as the temperature of 750 °C was attained, the heating system of the furnace was switched off and the sample was cooled down to room temperature within the furnace (samples referred to as NiA750C-0min and NiX750C-0min).

As known, the above process leads to the formation of Ni-rich magnetic nanoparticles in the zeolite structure [19,23].

3. Characterization techniques

Atomic absorption spectrophotometric (AAS) measurements were done using a PerkinElmer Analyst 100 apparatus [28,29] on materials dissolved in a 40 wt% HF and 14 wt% $HClO_4$ aqueous solution, with the aim to determine the Ni^{2+} and (residual) Na^{+} contents of Ni-exchanged A and X zeolites [28,29].

X-Ray Powder Diffraction (XRPD) measurements were performed at the beamline XPRESS, Elettra synchrotron, Italy. Samples were ground and high purity α-Al_2O_3 was added (10 wt%) as internal standard to carry out the amorphous phase quantification using the combined Rietveld and reference intensity ratio (RIR) method [30]. Final powders were packed into borosilicate glass capillaries and collected in Debye-Scherrer geometry. Diffraction intensities were recorded from 1.65° to 28.35° 2θ by an image plate MAR345 with a wavelength of 0.4957 Å. Dioptase software [31] was used to integrate collected images, while data analysis was performed using GSAS package [32] with EXPGUI interface [33].

Transmission electron microscopy (TEM) images were obtained using a JEOL 3010-UHR instrument operating at 300 kV and a FEI-TECNAI instrument operating at 120 kV, both equipped with a LaB_6 filament. To obtain a good dispersion of the sample particles, the powders were either briefly contacted with the lacey carbon Cu grids, resulting in the adhesion of some particles to the sample holder by mere electrostatic interactions or by dispersing the powder in ethanol and drop it on carbon Cu grids.

Magnetic hysteresis loop of all samples have been measured in the temperature range 5–300 K and in the field interval −70 - +70 kOe by means of a SQUID magnetometer subtracting all diamagnetic signals from the zeolitic host matrix and the sample holder. FC/ZFC magnetization curves were measured between 2 K and T_{MAX} = 300 K using the same setup under a field of 50 Oe with a heating rate of 6 K/min.

4. Results

4.1. Chemical composition

According to AAS chemical analysis, the Ni^{2+} exchanged zeolite A sample contains 0.30 $meqg^{-1}$ Fe^{2+} and 5.18 $meqg^{-1}$ Na^{+}, and the Ni^{2+} exchanged zeolite X sample contains 0.43 $meqg^{-1}$ Fe^{2+} and 4.31 $meqg^{-1}$ Na^{+}. The corresponding cation equivalent fractions were calculated to be: $x_{Ni} = 0.05$ and $x_{Na} = 0.95$ (Ni^{2+} exchanged zeolite A sample), and $x_{Ni} = 0.09$ and $x_{Na} = 0.91$(Ni^{2+} exchanged zeolite X sample).

The weight percentage of Ni in the final nanocomposites were calculated on the basis of the Ni^{2+} content of the exchanged zeolites, considering the final nanocomposites as completely dehydrated materials. Such weight percentage turned out to be $\alpha_0^* = 1.03$ and $\alpha_0^* = 1.68$ wt % in nanocomposite samples derived from A and X zeolites, respectively, as reported in Table 1, first column.

4.2. Structural characterization

4.2.1. XRPD

Three samples (Ni-exchanged A zeolites treated at 735 and 750 °C and Ni-exchanged X zeolite treated at 750 °C) were analyzed and the respective amorphous content determined. Diffraction patterns are reported in Fig. 1.

Structures of the original Ni-exchanged zeolites were used to fit the patterns of the thermally-treated samples. Only reflections belonging

Table 1

Sample		J = 1			J = 4		
	α_0 [a]	α_0	f_0	χ^2	α_0	f_0	χ^2
NiA735C-12min	0.0103	0.00905	0.056	4.09×10^{-5}	0.00872	0.025	1.99×10^{-4}
NiA750C-0min	0.0103	0.00885	0.065	4.48×10^{-4}	0.00846	0.025	6.79×10^{-4}
NiX735C-12min	0.0168	0.01290	0.045	3.46×10^{-4}	0.01257	0.015	5.21×10^{-4}
NiX750C-0min	0.0168	0.01180	0.145	1.53×10^{-3}	0.01074	0.055	3.31×10^{-3}

[a] From chemical composition analysis.

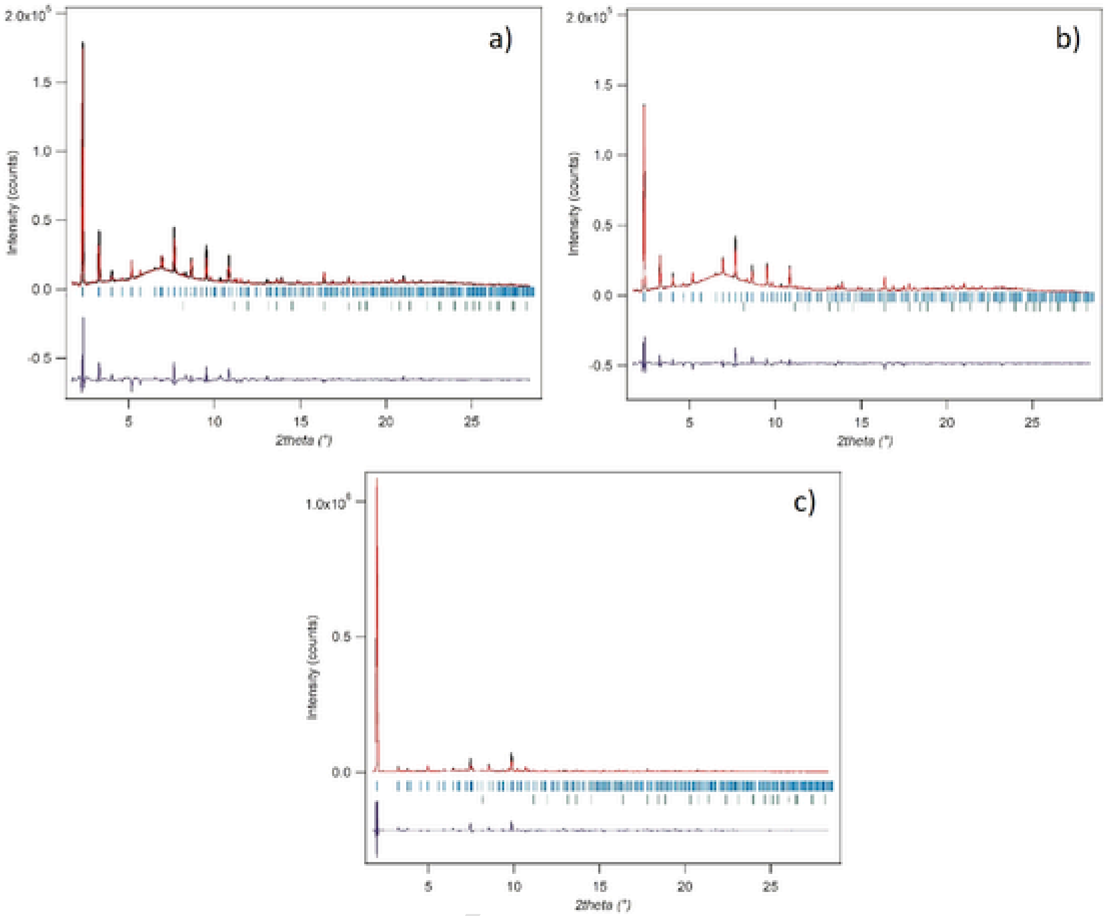

Fig. 1. Observed (black lines) and calculated (red lines) diffraction patters and final difference curve (blue line) from Rietveld refinements of samples NiA735C-12min (a), NiA750C-0min C° (b) and NiX750C-0min (c). Tick marks refer the different phases: green: α-Al_2O_3 standard; cyan: NiA (a and b) and NiX (c). (For interpretation of the references to color in this figure legend, the reader is referred to the Web version of this article.)

to the two zeolites and the internal standard (α-Al_2O_3) were observed. Indeed, despite TEM analysis shows the presence of Ni-rich particles (*vide infra*), their amount is not sufficiently high to be detected by the XRPD. Amorphous phase was quantified as equal to zero (estimated standard deviation: ±1 wt %) in all the investigated samples. This indicates that the thermal treatment does not result in thermal collapse of the microporous zeolite structure and therefore does not induce amorphization of Ni-exchanged zeolites, differently what observed in samples containing a larger amount of Ni [23].

4.2.2. TEM analysis

Typical TEM images of Ni-exchanged A/X zeolites after thermal treatment are shown in Fig. 2. The parent zeolite structure appears to be virtually unaffected by thermal treatment, in agreement with the evidence provided by XRPD. Frequency histograms are shown as insets. Generally speaking, Ni-rich nanoparticles larger than 10 nm occur in large assemblies at zeolite grain boundaries and/or surfaces, as expected considering that the small diameter of zeolite pores prevents the formation of large particles inside the grains; however, homogeneity and size distribution of nanoparticles are different from sample to sample.

In particular:

- sample NiA750C-0min is characterized by homogeneous nanoparticles (Fig. 2a and b) with sizes distributed in the range 10–35 nm (Fig. 2c). Mean nanoparticle size: 15.0 nm, mean magnetic volume: 3950 nm^3
- sample NiA735C-12min shows a similar homogeneous distribution (Fig. 2d and e) with a small tail in the 40–60 nm range (Fig. 2f); mean size: 16.5 nm, mean magnetic volume: 4955 nm^3.
- in sample NiX750C-0min many zeolite grain boundaries are not decorated with nanoparticles (Fig. 2i); most nanoparticles are regularly distributed in the 10–25 nm range (Fig. 2g and h) but a significant fraction are in the range 40–70 nm (inset of Fig. 2i; a single large nanoparticle is shown in Fig. 2h); mean size: 17.5 nm, mean magnetic volume: 9429 nm^3;
- sample NiX735C-12min is similarly characterized by many zeolite grain boundaries not decorated with nanoparticles (Figure 2n); most nanoparticles are in the 10–40 nm range (Figure 2l,m) with a rare occurrence of larger particles (inset in Figure 2n); mean size: 18 nm, mean magnetic volume: 7730 nm^3.

The differences observed in homogeneity and size distribution in the two families of samples derived from A/X zeolites are presumably related to the different structure of the parent materials. Likewise, in nanocomposites obtained by the same method and containing higher amounts of either Ni or Fe [22] a different size distribution of the metal NPs was observed in the nanocomposites obtained from either A or X zeolite.

4.3. Magnetic measurements

The hysteresis loops of two samples representative of all studied materials are shown in Fig. 3. The insets show details of the loops

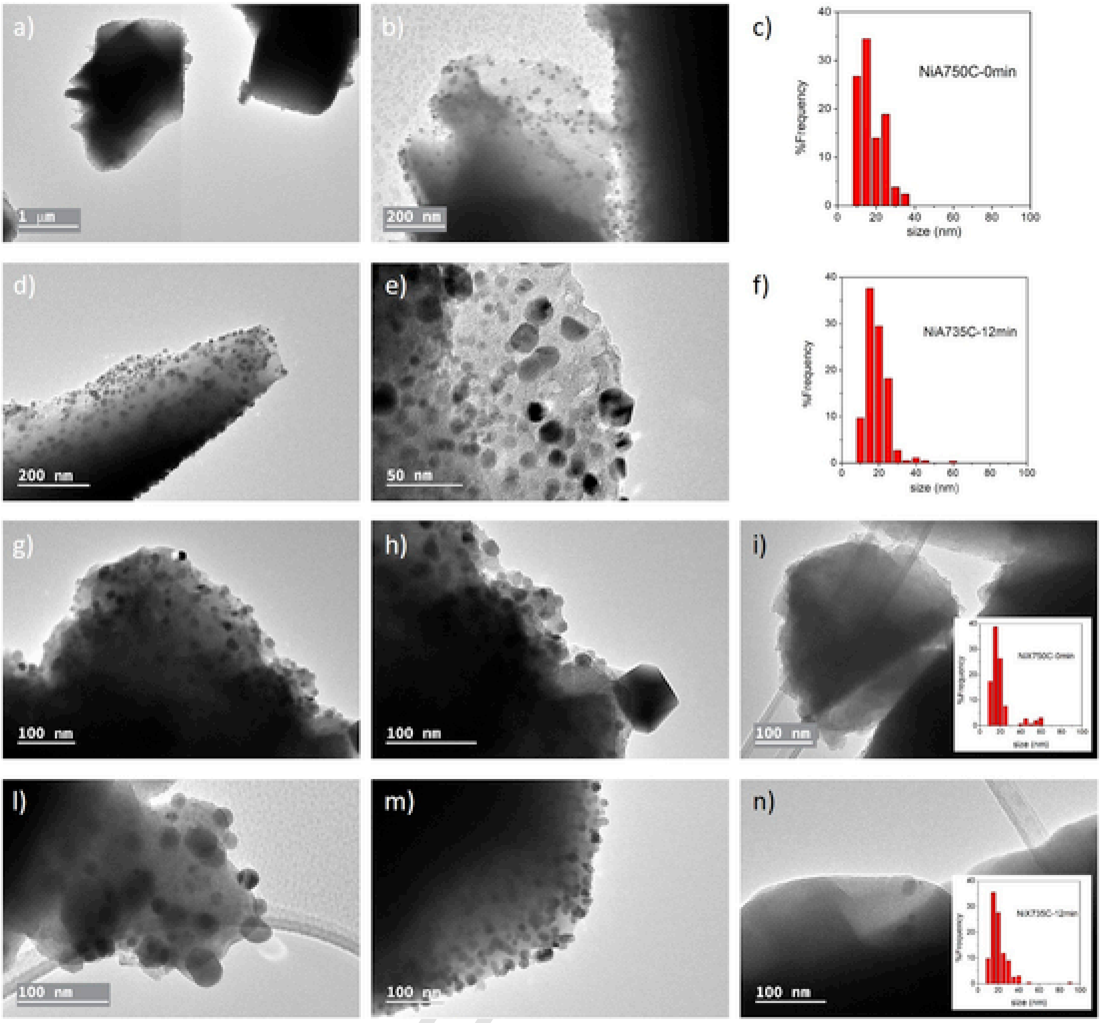

Fig. 2. Typical TEM images (a,b) and particle size distribution (c) of sample NiA750C-0min; (b–d): the same for sample NiA735C-12 min; grain surfaces with (g,h) and without (i) nanoparticles and particle size distribution (inset in panel (i)) of sample NiX750C_0min; (l-n and inset of panel (n)): the same for sample NiX735-12min.

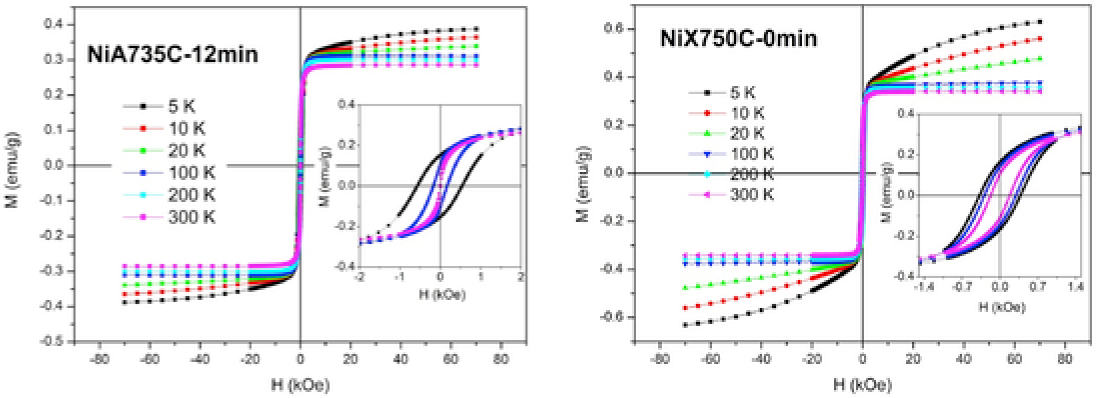

Fig. 3. Magnetic hysteresis loops measured in two representative samples between 5 and 300 K in the field interval ±70 kOe. Insets show in detail the changes of shape, coercive field and magnetic remanence at three temperatures (colors as indicated in the main frames). (For interpretation of the references to color in this figure legend, the reader is referred to the Web version of this article.)

at low fields. In both cases, the loops measured between 100 K and room temperature are characterized by a fully saturating behavior; however, an unsaturating contribution appears below about 75 K and becomes increasingly larger with reducing the temperature. This effect is best viewed by plotting the magnetization at H = 70 kOe (M_{70kOe}) as a function of temperature, and corresponds to the upward change of slope observed in Fig. 4 for the same two samples (symbols). The reported curves are representative of all studied materials.

Generally speaking, the measured hysteresis loops are compatible with the presence of a substantial contribution from nanoparticles that saturates well below 70 kOe. However, the low-temperature behavior indicates that a residual fraction of loaded nickel has not been in-

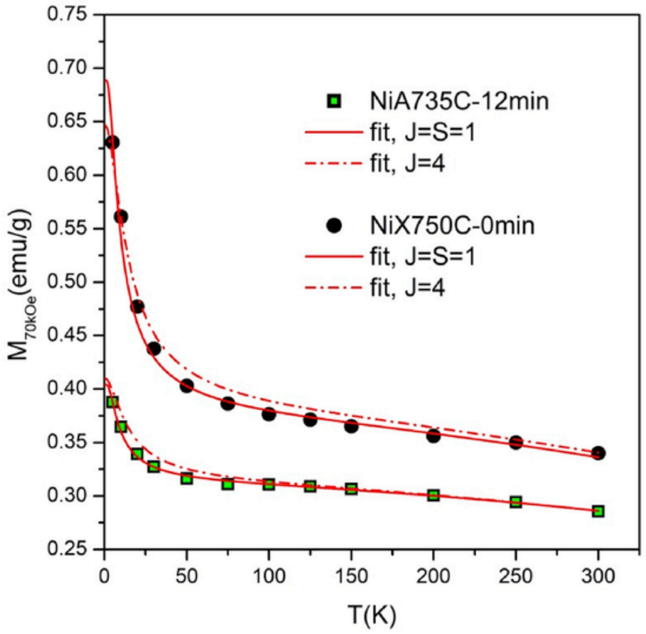

Fig. 4. Symbols: magnetization at H = 70 kOe ($M_{7\,kOe}$) as a function of temperature for the same samples as in Fig. 3. Full/dashed Lines: fitting curves obtained using Equation (4) with $J = 1$ and $J = 4$, respectively (see text for details).

cluded in nanoparticles and is present as Ni^{2+} ions dispersed in the host matrix, giving rise to a paramagnetic contribution. A similar residual fraction of magnetic ions was previously detected in materials derived from zeolite precursors loaded with a larger amount of Ni (15%) [23].

An antiferromagnetic phase with random anisotropy axes could, in principle, be responsible for the non-saturating magnetization trend observed at low temperatures; however, this cannot explain the downward curvature observed at low T in the high-field M(H) curves, which originates from the non-linear behavior of the a paramagnetic signal when the field is high enough and the temperature sufficiently low [34]. Moreover, the disappearance of the non-saturating signal in the high temperature limit is another fact pointing to a paramagnetic rather than antiferromagnetic effect.

The FC/ZFC curves of all materials are shown in Fig. 5 (left panel) after normalization to the value reached by the ZFC curve at $T_{MAX} = 300$ K. Because of the low applied field (50 Oe), these curves reflect the magnetic behavior of nanoparticles, the response from the ionic fraction being negligible even at the lowest investigated temperature. Generally speaking, all curves do not display the typical features expected from small superparamagnetic nanoparticles, i.e., a maximum of the ZFC curve occurring around the blocking temperature T_B, and an equilibrium region where FC and ZFC curves become merged [35]. In the present case, the ZFC curves display no maximum and the FC/ZFC curves always are separated, a small yet real gap between them occurring even at, the highest temperature reached in our measurements (T_{MAX}) as clearly shown in the top right panel of Fig. 5.

The two Ni-exchanged A zeolites exhibit a similar behavior, as well as the two Ni-exchanged X zeolites. In all cases, the shape of the curves is dictated by non-negligible interparticle interactions, expected for the nanoparticle assemblies put in evidence by TEM analysis. Interactions and large magnetic volumes (see previous Section) concur to determine T_B values well above T_{MAX}. As a matter of fact, the FC/ZFC curves of Ni-exchanged X zeolites appear to be flatter and featureless. This is presumably related to both a higher magnetic volume and a higher interparticle interaction, which derives from the higher inhomogeneity of nanoparticle distribution in space observed in the two samples obtained from X zeolite, where nanoparticles (basically similar in number to the A zeolite samples) are nevertheless present on a smaller number of grain surfaces/boundaries.

In fact, FC/ZFC curves of large, multidomain magnetic particles and/or strongly correlated nanoparticle aggregates are basically featureless [36–39]. When particles larger than 35 nm are not present, as in sample NiA750C-0min, the ZFC curve displays some curvature; such a feature is somewhat smoothed out in sample NiA735C-12min where a few 60-nm particles exist.

The gap between FC and ZFC curves at T_{MAX} is explained by a recent model based on a rate-equation approach [38] when the maximum measurement temperature T_{MAX} is below blocking temperature, as in the present case.

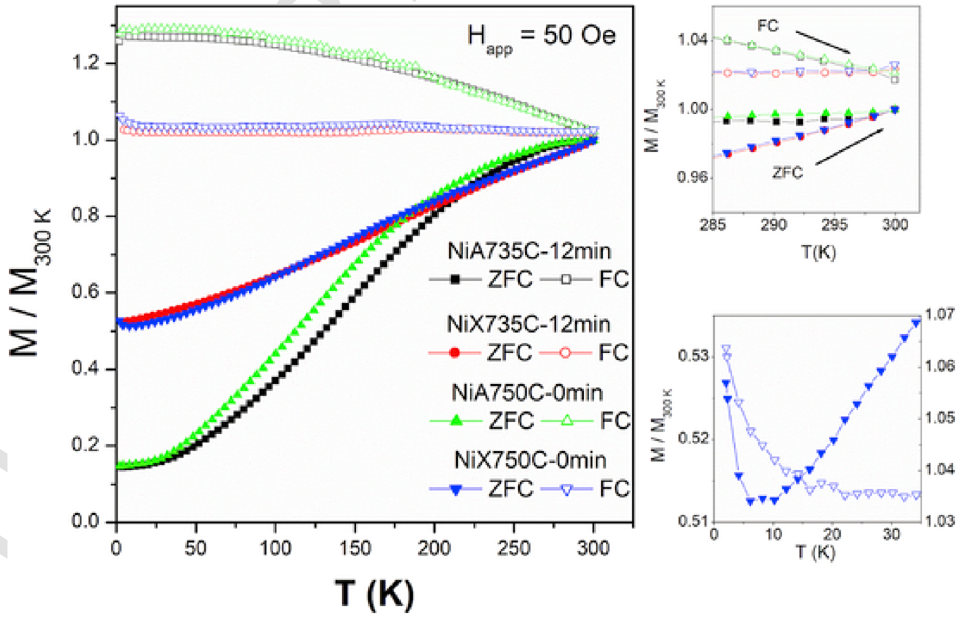

Fig. 5. Left panel: Normalized FC/ZFC curves measured in all studied samples. Upper right panel: detail of the high temperature region showing the gap between room-temperature magnetization values measured after completion of the ZFC and the FC curves. Lower right panel: low-temperature behavior of FC (open symbols) and ZFC (full symbols) curves of sample NiX750C-0min.

Both FC and ZFC curves measured on sample NiX750C-0min show a low temperature anomaly consisting in the increase of FC magnetization below about 15 K and a minimum of the ZFC curve around 8 K, as shown in the bottom right panel of Fig. 5. Such an effect, not appearing in the other three samples, is very similar to the low-temperature anomalies measured in materials derived from zeolite precursors loaded with ≈15% nickel [23], which were ascribed to the clustering of weakly interacting Ni^{2+} ions present in the matrix by effect of a ferrimagnetic interaction. The effect displayed by sample NiX750C-0min is much smaller than in materials loaded with a higher amount of Ni; the reason why the effect is not observed in the remaining three samples will be explained later.

The temperature dependence of the coercive field (H_c) is reported in Fig. 6 for all studied materials. Both samples obtained starting from A zeolites exhibit a very small coercive field H_c (<10 Oe) at room temperature and a steep increase with decreasing T, up to values of about 550 Oe at 5 K.

Such a behavior is compatible with the presence of nanoparticles with size in the 10–35 nm range. On the contrary, both samples obtained starting from X zeolites display a coercive field of about 200 Oe at room temperature and a weaker increase with decreasing T up to values of 350–380 Oe at 5 K, as expected in samples where large, multi-domain particles coexist together with smaller, single-domain nanoparticles.

These results indicate that the magnetic properties of the two samples obtained starting from A zeolites significantly differ from those of the other two samples; on the contrary, materials derived from X zeolites of the same type exhibit a closely similar behavior. This means that magnetic properties are more affected by the structure of the host material than by thermal treatment.

The magnetic analysis clearly shows that the Ni-rich nanoparticles observed by TEM are characterized by a ferromagnetic-like behavior up to room temperature, indicated by fully saturating *M(H)* curves at high fields (see Fig. 3). This leads us to exclude the presence of a dominant fraction of Ni oxides in nanoparticles, because its antiferromagnetic contribution [40,41] would result in a linear increase of the room-temperature *M(H)* curve at high fields, which is definitely not observed. On the other hand, magnetic measurements cannot exclude the presence of a nickel hydride phase, which may be characterized by a ferromagnetic behavior in nanoparticles [19]; however, it was shown that such a phase is either absent (in Ni-loaded X zeolites) or almost negligible (in Ni-loaded A zeolites) in materials produced by the same preparation process [19]. Therefore, it is suggested that the Ni-rich particles observed by TEM in the studied samples are basically composed of ferromagnetic, metallic Ni, as in the case of nanocomposites prepared with a larger amount of loaded Ni [23].

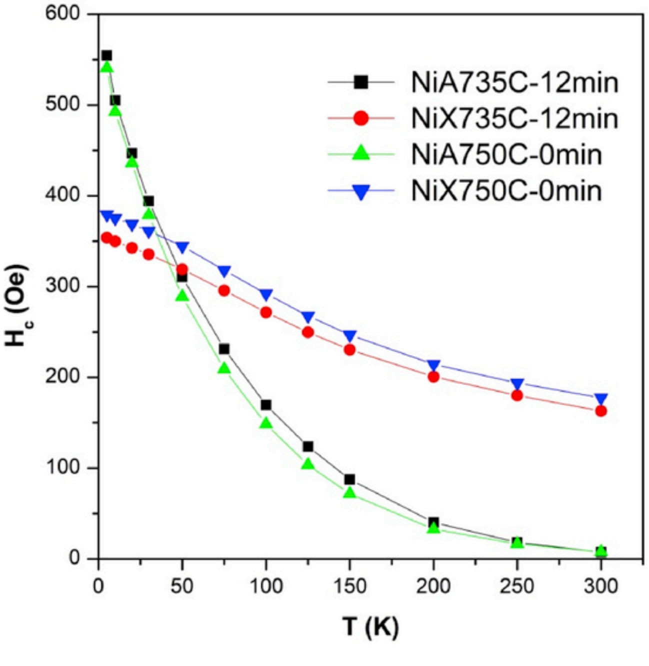

Fig. 6. Coercive field as a function of temperature for all studied samples.

4.4. Determining the ionic fraction

The data reported in Fig. 4 put in evidence the contribution of a Ni^{2+} ionic fraction responsible for the increase of M_{70kOe} at low temperatures. In materials derived from zeolite precursors loaded with a much larger amount of nickel [23] a specific procedure was conceived to get a figure of the residual ionic fraction *f* from combined analysis of structural and magnetic data. In the present case, the weak magnetic signals prevent us from directly applying the same procedure. However, a reasonably accurate estimate of *f* can be obtained on the basis of a few simplifying assumptions according to a self-consistent procedure outlined here.

The high-field magnetization M_{70kOe} at the lowest temperature attained in the measurements ($T_{\min} = 5$ K) is assumed to be the sum of independent contributions from Ni-rich nanoparticles and Ni^{2+} ions:

$$\begin{aligned} M_{70kOe}\left(T_{min}\right) &= M_{NP}\left(T_{min}\right) + M_{ion}\left(T_{min}\right) \\ &= (1-f)\,\alpha M^{*}_{NP}\left(T_{min}\right) \\ &\quad + Nf\mu_0 B_J\left(T_{min}\right) \end{aligned} \tag{1}$$

where *N* is the total number (per gram of loaded zeolite) of Ni atoms/ions present in the material and *f* is the fraction of paramagnetic Ni^{2+} ions ($0 \le f \le 1$). This assumption is supported by the fact that Ni-rich nanoparticles and residual Ni^{2+} ions are expected to be present in different regions, the latter being assumed to penetrate the zeolitic grains.

The term $M_{NP}(T_{\min})$ in Equation (1) represents the magnetic contribution of nanoparticles, α is the actual fraction of nickel with respect to the host zeolite (expected to be close to the nominal value), M^{*}_{NP} is the intrinsic magnetization of magnetic nanoparticles (per gram of Ni). We take here $M^{*}_{NP} = 36$ emu/g as in the particles present in zeolites containing ≈15% Ni [23,42]. Such a value is appropriate also in the presence of a fraction of ferromagnetic nickel hydride, because it has been experimentally shown that in nanoparticles the intrinsic magnetization of this compound is basically the same as the one of metallic Ni [19].

The product $(1-f)\,\alpha$ is the amount of Ni contained in the nanoparticle phase. It should be noted that α and N are proportional because $\alpha = N m_{Ni}$ where $m_{Ni} = 9.746 \times 10^{-23}$ g is the mass of a single atom/ion of nickel.

The second term of Equation (1) represents the contribution of paramagnetic ions of total angular momentum J and magnetic moment $\mu_0 = g_J J \mu_B$, B_J being the Brillouin's function at $H = 70$ kOe. The exact degree of orbital momentum quenching of Ni^{2+} ions determines their magnetic behavior. Actually, the degree of quenching is not known, although there are strong indications of incomplete or nearly complete orbital-momentum quenching in Ni^{2+} ions embedded in zeolite materials [23,43,44]. As a consequence, we have resolved to separately apply the procedure to the two extreme cases of no quenching ($J = 4$, $g_4 = 5/4$) and full quenching ($J = S = 1$, $g_1 = 2$) in order to establish the limits of validity of the results.

In Equation (1) the unknown is *f*; however, the total content of Ni (α) can be viewed *a priori* as an ill-known variable close to the value obtained from the chemical composition analysis. The procedure envisaged here to simultaneously obtain f and α from magnetic measurements makes use of the quantities defined in Fig. 7 (left panel),

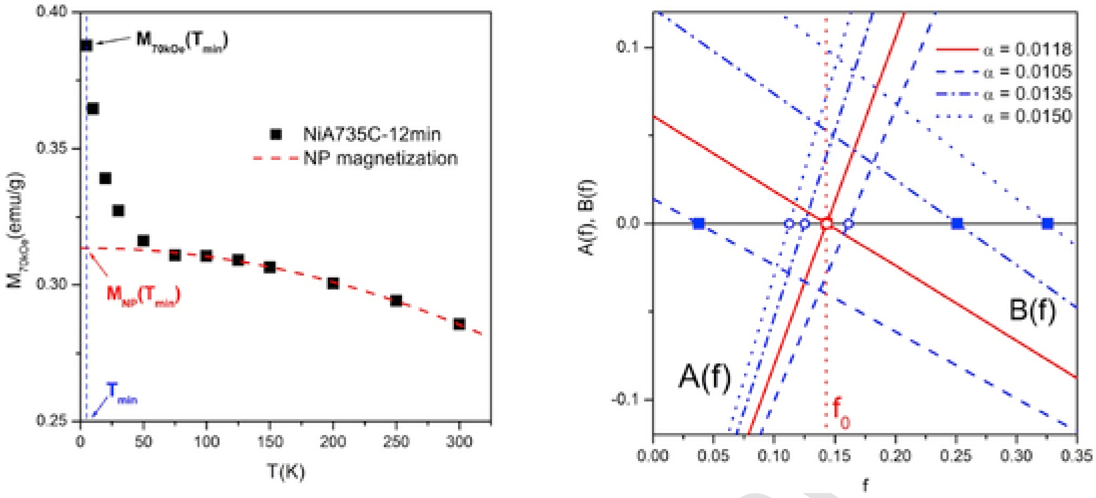

Fig. 7. Left panel: definition of the quantities used in the model (Equations (2) and (3)). Right panel: behavior of the A(f), B(f) functions defined in Equations (2) and (3) using α as a free parameter (see text).

i.e., the experimental value of M_{70kOe} ($T_{\min}$) and the estimated value of the magnetization of nanoparticles, M_{NP} ($T_{\min}$).

The latter quantity is obtained as follows: at high temperatures ($T > 100$ K) the experimental $M_{70kOe}(T)$ curve is dominated by the contribution from nanoparticles, the magnetic signal from paramagnetic ions being negligible there. The curve which fits the high-temperature magnetization (dashed red line in Fig. 7, left panel) is extrapolated down to $T_{\min}$ and the corresponding value is taken as a reasonable estimate of M_{NP} ($T_{\min}$). As a consequence, the ionic contribution at $T_{\min}$ is just $M_{ion}\left(T_{min}\right) = M_{70kOe}\left(T_{min}\right) - M_{NP}\left(T_{min}\right)$.

Using f as a free parameter, a starting guess of α is done. The following quantities are defined:

$$A\left(f\right) = \frac{\alpha}{m_{Ni}} f \mu_0 B_J\left(T_{min}\right) - M_{ion}\left(T_{min}\right) \tag{2}$$

$$B\left(f\right) = \left(1-f\right)\alpha M^{*}_{NP} - M_{NP}\left(T_{min}\right) \tag{3}$$

In both Equations for a given choice of J (equal to either 1 or 4) all parameters excepting f and α are experimentally known and fixed. One looks for a single value f_0 such that $A\left(f_0\right) = B\left(f_0\right) = 0$. When such a condition is fulfilled the two addends appearing in the last expression of Equation (1) become identically equal to the experimental values.

Both $A(f)$ and $B(f)$ are linear functions of f and cross the horizontal axis when f is varied between 0 and 1, as shown in the right panel of Fig. 7 for some values of α, in the case of full orbital-momentum quenching ($J = 1$).

For a generic value of α the two zeros of $A(f)$, $B(f)$ occur at different values of f, as shown in the same Figure (dashed, dotted and dash-dotted blue lines), so that the corresponding values of α are not acceptable. However, the zero of $A(f)$ moves towards higher f values with increasing α, the opposite being true for the zero of $B(f)$; by suitably changing α, it is possible to find a value α_0 such that the two zeros become coincident ($f = f_0$; red lines in Figure M5). The (f_0,α_0) pair corresponds to the solution.

The procedure is repeated for all materials and for the two limit values of the total angular momentum, $J = 1$ and $J = 4$. The results are reported in Table 1.

Table caption: Total Ni fraction α_0 and fraction of residual Ni^{2+} ions f_0, as obtained applying the procedure described in the text. The limiting cases of J = 1 and J = 4 (full quenching/no quenching of the orbital angular momentum of Ni ions) are separately treated. The quantity χ^2 is the Chi-square parameter resulting from fits of the high-field magnetization M_{70kOe} (T) to the theoretical curves obtained using the corresponding α_0 and f_0 values.

The following conclusions can be drawn: a) for both values of J, α_0 – as determined from magnetic measurements - turns out to be in satisfactory agreement with the results of chemical composition analysis (Table 1, first column); it is confirmed that the total nickel content in samples obtained from X zeolites is slightly larger than in the ones obtained from A zeolites; the largest ionic fraction is found in sample NiX750C-0min, for both choices of J. All values of f_0 are systematically smaller when $J = 4$. As anticipated, the values of α_0 and f_0 given in Table 1 should be merely viewed as indicative rather than definitive, because they have been obtained under two limit assumptions about the degree of orbital quenching of Ni^{2+} ions. In any case, a good agreement between the present results and experimental data is found by plotting the sample magnetization at T = 300 K as a function of the product α_0 (1- f_0), i.e., the fraction of Ni contained in the nanoparticles. Note that at room temperature the contribution of the ionic fraction is basically zero. The experimental data, shown in Fig. 8, are fitted by a linear law passing through the origin. The differences between the α_0 (1- f_0) values obtained in the two limit cases $J = 1$ and $J = 4$ are so small that the points are almost superimposed. The slope of the fitting straight line is equal to 33.96 emu/g, indicating that the saturation magnetization expected at 300 K in an ideal material entirely composed of Ni nanoparticles would be close to 34 emu/g, a quite reasonable value taking into account that the same quantity for bulk Ni is about 54 emu/g [34] and that M_s is always significantly lower in nanoparticles than in bulk materials [45].

It is possible to further check the adequacy of the data reported in Table 1 by fitting the experimental values of $M_{70kOe}(T)$ reported in Fig. 4 to the law:

$$M_{70kOe}\left(T\right) = \left(1-f_0\right)\alpha_0 M^{*}_{NP}\left(T\right) + \frac{\alpha_0}{m_{Ni}} f_0 \mu_0 B_J\left(T\right) \tag{4}$$

over the entire temperature range, using the values of Table 1 for f_0 and α_0. The fitting curves are shown by red full/dashed lines (for $J = 1$ and $J = 4$, respectively) in Fig. 4. Generally speaking, for both limit values of J the theoretical curves explain the experimental behavior of $M_{70kOe}(T)$. The same agreement is found in the two samples not shown in Figure. However, the fitting curves with $J = 1$ apparently reproduce the experimental data more accurately. This conclusion is substantiated by the smaller χ^2 parameter systematically exhibited by the curves obtained using $J = 1$ (see Table 1). It is suggested that the residual Ni^{2+} ions found in these materials exhibit a significant, albeit incom-

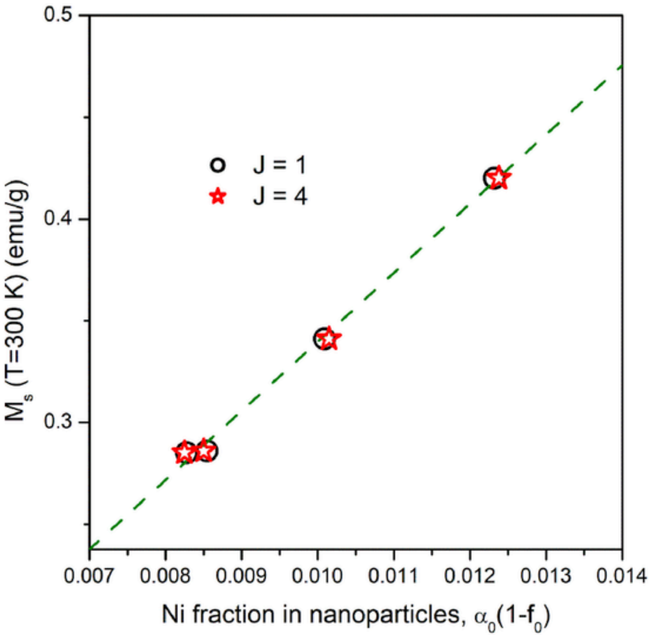

Fig. 8. Room-temperature magnetization measured in all studied samples plotted as a function of the fraction of Ni contained in the nanoparticles for both degrees of quenching ($J = 1,4$).

plete quenching of the orbital momentum, in line with previous findings [43,44].

The present analysis indicates that the annealing treatment has weak or no effects on the ionic fraction in samples obtained from A zeolites, whereas samples obtained from X zeolites are more significantly affected. The residual ionic fraction turns out to be substantially higher in sample NiX750C-0min than in all other materials. This result explains why the low temperature anomaly in the FC/ZFC curve (Fig. 5, bottom right panel) is observed in this sample only. A closely similar anomaly was already detected in samples containing 15% Ni [23], and interpreted in terms of low-temperature clustering of weakly interacting Ni^{2+} ions. In the present samples, the few paramagnetic ions can be figured out as mainly non-interacting; however, when f_0 is sufficiently high as in sample NiX750C-0min, magnetic interactions among ions begins to play some role. Using the procedure of analysis and the interpretation scheme developed elsewhere [23], it is possible to single out the response of magnetic clusters created at very low temperature by ferrimagnetic interaction among ions; the result is reported in Fig. S1 of the Supplementary Material. The analysis shows that magnetic clusters in sample NiX750C-0min gradually lose their identity above 30 K, as found in materials derived from zeolite precursors containing ≈15% Ni [23]; however, the blocking temperature of these clusters is very small (below 2 K, as proven by the absence of a maximum in the subtracted ZFC curve of Fig. S1) so that the mean energy barrier height arising from magnetic interactions is much smaller than in materials with a higher Ni content.

The quantitative results about the fractions of Ni ions and of Ni-rich nanoparticles reported in Table 1 are based on a self-consistent analysis of magnetic data; an accurate cross-check of the method's validity by comparison with other experimental methods is made particularly difficult by the sensitivity limits of the conventional techniques of structural analysis, which prevent one to draw reliable conclusions in this case, because of the very low amount of loaded Ni. Specific advanced techniques could be envisaged, such as spin-dependent spectroscopic techniques or atomic resolution HRTEM, which would be able - under particular conditions and in accurately prepared samples - to resolve single atoms in a structure, thus allowing one to get independent information about the fraction of Ni ions in the zeolitic cage. However, these techniques are expected to provide unambiguous results when applied to systems compositionally/morphologically much simpler than the present nanocomposites.

5. Conclusions

Magnetic nanocomposites based on A/X zeolites loaded with a small amount of Ni (≅ 1 wt%) have been obtained by making use of a process involving ionic exchange of parent zeolites with a [Ni^{2+}] solution, followed by thermal treatments.

Ni-rich nanoparticles in the 10–80 nm range appear after thermal treatment at the boundaries/surfaces of zeolite grains; however, a fraction of exchanged Ni^{2+} ions still remains inside grains. It has been shown that:

a) the distribution in space and size of nanoparticles is significantly affected by the type of parent zeolite, a more homogeneous distributions being found in A zeolite;
b) magnetic nanoparticles are interacting and their blocking temperature is well above room temperature;
c) the relative amount of Ni present as ionic fraction (f_0) can be determined by exploiting an *ad-hoc* method of analysis;
e) the experimental high-field *M(T)* curves are better fitted assuming full quenching of the orbital momentum of dilute Ni^{2+} ions.
f) when the concentration of residual magnetic ions is large enough, magnetic clusters appear at very low temperature by effect of weak interactions among ions.

The present work shows how magnetic measurements supported by structural/morphologic observations may allow one to study elusive compositional details in weakly loaded magnetic nanocomposites where standard characterization methods may not be able to provide clear information.

Appendix A. Supplementary data

Supplementary data to this article can be found online at https://doi.org/10.1016/j.jallcom.2019.152776.

References

[1] R.D. Ambashta, M. Sillanpää, Water purification using magnetic assistance: a review, J. Hazard Mater. 180 (2010) 38–49, doi:10.1016/J.JHAZMAT.2010.04.105.

[2] J. Zhu, S. Wei, M. Chen, H. Gu, S.B. Rapole, S. Pallavkar, T.C. Ho, J. Hopper, Z. Guo, Magnetic nanocomposites for environmental remediation, Adv. Powder Technol. 24 (2013) 459–467, doi:10.1016/J.APT.2012.10.012.

[3] M. Brigante, E. Pecini, M. Avena, Magnetic mesoporous silica for water remediation: synthesis, characterization and application as adsorbent of molecules and ions of environmental concern, Microporous Mesoporous Mater. 230 (2016) 1–10, doi:10.1016/J.MICROMESO.2016.04.032.

[4] C. Tang, Y.H. Huang, H. Zeng, Z. Zhang, Reductive removal of selenate by zero-valent iron: the roles of aqueous Fe^{2+} and corrosion products, and selenate removal mechanisms, Water Res. 67 (2014) 166–174, doi:10.1016/J.WATRES.2014.09.016.

[5] L. Ling, B. Pan, W. Zhang, Removal of selenium from water with nanoscale zero-valent iron: mechanisms of intraparticle reduction of Se(IV), Water Res. 71 (2015) 274–281, doi:10.1016/J.WATRES.2015.01.002.

[6] C. Tang, Y. Huang, Z. Zhang, J. Chen, H. Zeng, Y.H. Huang, Rapid removal of selenate in a zero-valent iron/Fe_3O_4/Fe^{2+} synergetic system, Appl. Catal. B Environ. 184 (2016) 320–327, doi:10.1016/J.APCATB.2015.11.045.

[7] Y. Sun, S.S. Chen, D.C.W. Tsang, N.J.D. Graham, Y.S. Ok, Y. Feng, X.-D. Li, Zero-valent iron for the abatement of arsenate and selenate from flowback water of hydraulic fracturing, Chemosphere 167 (2017) 163–170, doi:10.1016/J.CHEMOSPHERE.2016.09.120.

[8] Z. Ma, C. Shan, J. Liang, M. Tong, Efficient adsorption of Selenium(IV) from water by hematite modified magnetic nanoparticles, Chemosphere 193 (2018) 134–141, doi:10.1016/J.CHEMOSPHERE.2017.11.005.

[9] A.A. Mirzaei, A. Being babaei, M. Galavy, A. Youssefi, A silica supported Fe–Co bimetallic catalyst prepared by the sol/gel technique: operating conditions, catalytic properties and characterization, Fuel Process. Technol. 91 (2010) 335–347, doi:10.1016/J.FUPROC.2009.11.005.

[10] N.D. Meeks, V. Smuleac, C. Stevens, D. Bhattacharyya, Iron-based nanoparticles for toxic organic degradation: silica platform and green synthesis, Ind. Eng. Chem. Res. 51 (2012) 9581–9590, doi:10.1021/ie301031u.

[11] K. Keyvanloo, M.K. Mardkhe, T.M. Alam, C.H. Bartholomew, B.F. Woodfield, W.C. Hecker, Supported iron fischer–tropsch catalyst: superior activity and stability using a thermally stable silica-doped alumina support, ACS Catal. 4 (2014) 1071–1077, doi:10.1021/cs401242d.

[12] B. Liu, Z. Zhang, Catalytic conversion of biomass into chemicals and fuels over magnetic catalysts, ACS Catal. 6 (2016) 326–338, doi:10.1021/acscatal.5b02094.

[13] A.K. Gupta, M. Gupta, Synthesis and surface engineering of iron oxide nanoparticles for biomedical applications, Biomaterials 26 (2005) 3995–4021, doi:10.1016/J.BIOMATERIALS.2004.10.012.

[14] M. Chao, L. Chuanyan, H. Nongyue, W. Fang, M. Ningning, Z. Liming, L. Zhuoxuan, A. Zeeshan, X. Zhijiang, L. Xiaolong, L. Gaofeng, L. Hongna, D. Yan, X. Lijian, W. Zhifei, Preparation and characterization of monodisperse core–shell $Fe_3O_4@SiO_2$ microspheres and its application for magnetic separation of nucleic acids from E. coli BL21, J. Biomed. Nanotechnol. 8 (2012) 1000–1005, doi:10.1166/jbn.2012.1454.

[15] A.-H. Lu, E.L. Salabas, F. Schüth, Magnetic nanoparticles: synthesis, protection, functionalization, and application, Angew. Chem. Int. Ed. 46 (2007) 1222–1244, doi:10.1002/anie.200602866.

[16] S. Esposito, A. Marocco, B. Bonelli, M. Pansini, Produzione di materiali compositi metallo-ceramici nano strutturati da precursori zeolitici, MI 2014 A 000522, 2014.

[17] S. Esposito, A. Marocco, B. Bonelli, M. Pansini, Production of magnetic metal nanoparticles embedded in a silica-alumina matrix, PCT Int. Appl. Publ. (2015) WO 2015/145230 A1.

[18] A. Marocco, G. Dell'Agli, S. Esposito, M. Pansini, Metal-ceramic composite materials from zeolite precursor, Solid State Sci. 14 (2012) 394–400, doi:10.1016/J.SOLIDSTATESCIENCES.2012.01.006.

[19] S. Esposito, G. Dell'Agli, A. Marocco, B. Bonelli, P. Allia, P. Tiberto, G. Barrera, M. Manzoli, R. Arletti, M. Pansini, Magnetic metal-ceramic nanocomposites obtained from cation-exchanged zeolite by heat treatment in reducing atmosphere, Microporous Mesoporous Mater. 268 (2018) 131–143, doi:10.1016/J.MICROMESO.2018.04.024.

[20] M. Pansini, G. Dell'Agli, A. Marocco, P.A.P.A. Netti, E. Battista, V. Lettera, P. Vergara, P. Allia, B. Bonelli, P. Tiberto, G. Barrera, G. Alberto, G. Martra, R. Arletti, S. Esposito, Preparation and characterization of magnetic and porous metal-ceramic nanocomposites from a zeolite precursor and their application for DNA separation, J. Biomed. Nanotechnol. 13 (2017) 337–348, doi:10.1166/jbn.2017.2345.

[21] M. Pansini, F. Sannino, A. Marocco, P. Allia, P. Tiberto, G. Barrera, M. Polisi, E. Battista, P.A. Netti, S. Esposito, Novel process to prepare magnetic metal-ceramic nanocomposites from zeolite precursor and their use as adsorbent of agrochemicals from water, J. Environ. Chem. Eng. 6 (2018), doi:10.1016/j.jece.2017.12.030.

[22] F.S. Freyria, A. Marocco, S. Esposito, B. Bonelli, G. Barrera, P. Tiberto, P. Allia, P. Oudayer, A. Roggero, J.-C. Matéo-Vélez, E. Dantras, M. Pansini, Simulated moon agglutinates obtained from zeolite precursor by means of a low-cost and scalable synthesis method, ACS Earth Space Chem. (2019) acsearthspacechem.9b00042, doi:10.1021/acsearthspacechem.9b00042.

[23] G. Barrera, P. Tiberto, S. Esposito, A. Marocco, B. Bonelli, M. Pansini, M. Manzoli, P. Allia, Magnetic clustering of Ni^{2+} ions in metal-ceramic nanocomposites obtained from Ni-exchanged zeolite precursors, Ceram. Int. 44 (2018) 17240–17250, doi:10.1016/j.ceramint.2018.06.182.

[24] G. Barrera, P. Tiberto, P. Allia, B. Bonelli, S. Esposito, A. Marocco, M. Pansini, Y. Leterrier, Magnetic properties of nanocomposites, Appl. Sci. 9 (2019) 212, doi:10.3390/app9020212.

[25] A. Marocco, G. Dell'Agli, L. Spiridigliozzi, S. Esposito, M. Pansini, The multifarious aspects of the thermal conversion of Ba-exchanged zeolite A to monoclinic celsian, Microporous Mesoporous Mater. 256 (2018) 235–250, doi:10.1016/J.MICROMESO.2017.08.018.

[26] A. Marocco, G. Dell'Agli, S. Esposito, M. Pansini, The role of residual Na^+ and Li^+ on the thermal transformation of Ba-exchanged zeolite A, Solid State Sci. 13 (2011) 1143–1151, doi:10.1016/J.SOLIDSTATESCIENCES.2011.01.002.

[27] S. Esposito, A. Marocco, G. Dell'Agli, B. De Gennaro, M. Pansini, Relationships between the water content of zeolites and their cation population, Microporous Mesoporous Mater. 202 (2015) 36–43, doi:10.1016/J.MICROMESO.2014.09.041.

[28] A. Marocco, B. Liguori, G. Dell'Agli, M. Pansini, Sintering behaviour of celsian based ceramics obtained from the thermal conversion of (Ba, Sr)-exchanged zeolite A, J. Eur. Ceram. Soc. 31 (2011) 1965–1973, doi:10.1016/J.JEURCERAMSOC.2011.04.028.

[29] G. Dell'Agli, C. Ferone, G. Mascolo, M. Pansini, Crystallization of monoclinic zirconia from metastable phases, Solid State Ion. 127 (2000) 223–230, doi:10.1016/S0167-2738(99)00279-9.

[30] A.F. Gualtieri, IUCr, Accuracy of XRPD QPA using the combined Rietveld–RIR method, J. Appl. Crystallogr. 33 (2000) 267–278, doi:10.1107/S002188989901643X.

[31] C. Prescher, V.B. Prakapenka, *DIOPTAS*: a program for reduction of two-dimensional X-ray diffraction data and data exploration, High Press. Res. 35 (2015) 223–230, doi:10.1080/08957959.2015.1059835.

[32] C.A. Larson, R.B. Von Dreele, General Structure Analysis System "GSAS,", Los Alamos, 1994.

[33] B.H. Toby, IUCr, *EXPGUI* , a graphical user interface for *GSAS*, J. Appl. Crystallogr. 34 (2001) 210–213, doi:10.1107/S0021889801002242.

[34] B.D. Cullity, C.D. Graham, Introduction to Magnetic Materials, 2009.

[35] M. Knobel, W.C. Nunes, L.M. Socolovsky, E. De Biasi, J.M. Vargas, J.C. Denardin, Superparamagnetism and other magnetic features in granular materials: a review on ideal and real systems, J. Nanosci. Nanotechnol. 8 (2008) 2836–2857, doi:10.1166/jnn.2008.15348.

[36] G. Barrera, C. Sciancalepore, M. Messori, P. Allia, P. Tiberto, F. Bondioli, Magnetite-epoxy nanocomposites obtained by the reactive suspension method: microstructural, thermo-mechanical and magnetic properties, Eur. Polym. J. 94 (2017) 354–365, doi:10.1016/j.eurpolymj.2017.07.022.

[37] D. Caruntu, G. Caruntu, C.J. O'Connor, Magnetic properties of variable-sized Fe_3O_4 nanoparticles synthesized from non-aqueous homogeneous solutions of polyols, J. Phys. D Appl. Phys. 40 (2007) 5801–5809, doi:10.1088/0022-3727/40/19/001.

[38] P. Allia, G. Barrera, P. Tiberto, Linearized rate-equation approach for double-well systems: cooling- and temperature-dependent low-field magnetization of magnetic nanoparticles, Phys. Rev. B. 98 (2018) 134423, doi:10.1103/PhysRevB.98.134423.

[39] M. Uva, L. Mencuccini, A. Atrei, C. Innocenti, E. Fantechi, C. Sangregorio, M. Maglio, M. Fini, R. Barbucci, On the mechanism of drug release from polysaccharide hydrogels cross-linked with magnetite nanoparticles by applying alternating magnetic fields: the case of DOXO delivery, Gels 1 (2015) 24–43, doi:10.3390/gels1010024.

[40] K. Nadeem, A. Ullah, M. Mushtaq, M. Kamran, S.S. Hussain, M. Mumtaz, Effect of air annealing on structural and magnetic properties of Ni/NiO nanoparticles, J. Magn. Magn. Mater. 417 (2016) 6–10, doi:10.1016/j.jmmm.2016.05.064.

[41] A. Jafari, S. Pilban Jahromi, K. Boustani, B.T. Goh, N.M. Huang, Evolution of structural and magnetic properties of nickel oxide nanoparticles: influence of annealing ambient and temperature, J. Magn. Magn. Mater. 469 (2019) 383–390, doi:10.1016/j.jmmm.2018.08.005.

[42] W. Gong, H. Li, Z. Zhao, J. Chen, Ultrafine particles of Fe, Co, and Ni ferromagnetic metals, J. Appl. Phys. 69 (1991) 5119–5121, doi:10.1063/1.348144.

[43] M.D. Mukadam, S.M. Yusuf, R. Sasikala, T. Ni, Magnetic properties of Ni^{2+} clusters in NaY zeolite, J. Appl. Phys. 103902 (2007) 1–5, doi:10.1063/1.2815624.

[44] S. Matsuo, S. Satou, M. Suzuki, M. Sano, H. Nakano, Magnetic properties of small nickel oxide clusters enclosed in Y-zeolite, Atoms, Mol. Clust. 285 (1991) 281–285.

[45] C. Sciancalepore, A.F. Gualtieri, P. Scardi, A. Flor, P. Allia, P. Tiberto, G. Barrera, M. Messori, F. Bondioli, Structural characterization and functional correlation of Fe_3O_4 nanocrystals obtained using 2-ethyl-1,3-hexanediol as innovative reactive solvent in non-hydrolytic sol-gel synthesis, Mater. Chem. Phys. 207 (2018) 337–349, doi:10.1016/j.matchemphys.2017.12.089.